Supporting Information

Investigating the Abnormal Conductivity Behaviour of Divalent Cations in Low Dielectric Constant Tetraglyme-Based Electrolytes

Long Hoang Bao Nguyen [a#], Tanguy Picard [b#], Cristina Iojoiu [b,c]*, Fannie Alloin [b,c], Nicolas Sergent [b], Marie-Liesse Doublet [a,c]*, and Jean-Sébastien Filhol [a,c]*

[a] ICGM, Univ Montpellier, CNRS, ENSCM, Montpellier, France

[b] Univ. Grenoble Alpes, Univ. Savoie Mont Blanc, CNRS, Grenoble INP, LEPMI, 38000 Grenoble, France

[c] RS2E French Network on Electrochemical Energy Storage, FR5439, Amiens, France

Corresponding authors:

Cristina Iojoiu (cristina.iojoiu@grenoble-inp.fr)

Marie-Liesse Doublet (Marie-Liesse.Doublet@umontpellier.fr)

Jean-Sébastien Filhol (Jean-Sebastien.Filhol@umontpellier.fr)

[#]: Authors contributed equally

Experimental and Calculation Methods

Sample preparation. All electrolytes were prepared from Calcium (II) Bis(trifluoromethanesulfonyl)imide (Ca(TFSI)$_2$) purchased from TCI Chemical, dried 48h under vacuum at 80°C and stored in an Ar-filled glove box. 2 mL solutions were prepared with tetraethylene glycol dimethyl ether ($\geq$ 99%) purchased from Merck (i.e. H$_3$CO(CH$_2$CH$_2$O)$_4$CH$_3$ or tetraglyme/G4), distilled under vacuum, and kept in an Ar-filled glovebox on molecular sieves to suppress water presence and other impurities from commercial solvent. The water content in electrolytes was below 60 ppm, as assessed by Karl-Fischer titration.

Electric measurements. The solution ionic conductivity was determined by Electrochemical Impedance Spectroscopy (EIS). The measurement was performed under potentiostatic conditions using the HP model 4192A LF impedance analyser. An exciting potential of 50 mV was applied in the frequency range of 13 MHz to 1 Hz. Results were fit using Z-view software. The Radiometer analytical conductivity cells filled with the electrolyte were hermetically sealed and put in an oven (VTM 4004, Vötsch). The cell factor was previously determined using KCl solutions of known ionic conductivity. Measurements were performed every 10°C from 20°C to 90°C, and then every 5°C when cooling from 90°C to -20°C to evaluate hysteresis phenomena. In order to model EIS data, the least square method written with the python Scipy solver was used. The parameter standard deviation errors (computed from covariance matrix) were 4% on average.

Viscosity measurement. Viscosity measurements were carried on an ARES-G2 rheometer from TA instruments (New Castel, PA, USA). The sample was placed in a Peltier device of 50 mm diameter. Viscosity was measured at constant shear rate of 100 Hz. Measurements were performed every 5°C from 20 to 90°C; two measurements were carried out at every temperature.

Differential scanning calorimetry. DSC measurements were carried on a Mettler-Toledo DSC1 star system between -150°C and 100°C with a cooling and heating rate of 10 K·min^{-1}. All the measured samples were prepared in an Ar-filled glovebox. The usual mass of a sample was ~ 4 mg.

Raman spectroscopy. Raman scattering was measured at the 785 nm excitation line of a laser diode using a Renishaw Invia spectrometer equipped with a Peltier cooled CCD. Measurement in macro-Raman configuration was carried on 2 mL solutions through an Ar-filled glass flask sealed with a cap. The background contribution of the glass container was subtracted from the sample spectrum, and the modelling tools available in Renishaw Wire 3.0 software were used
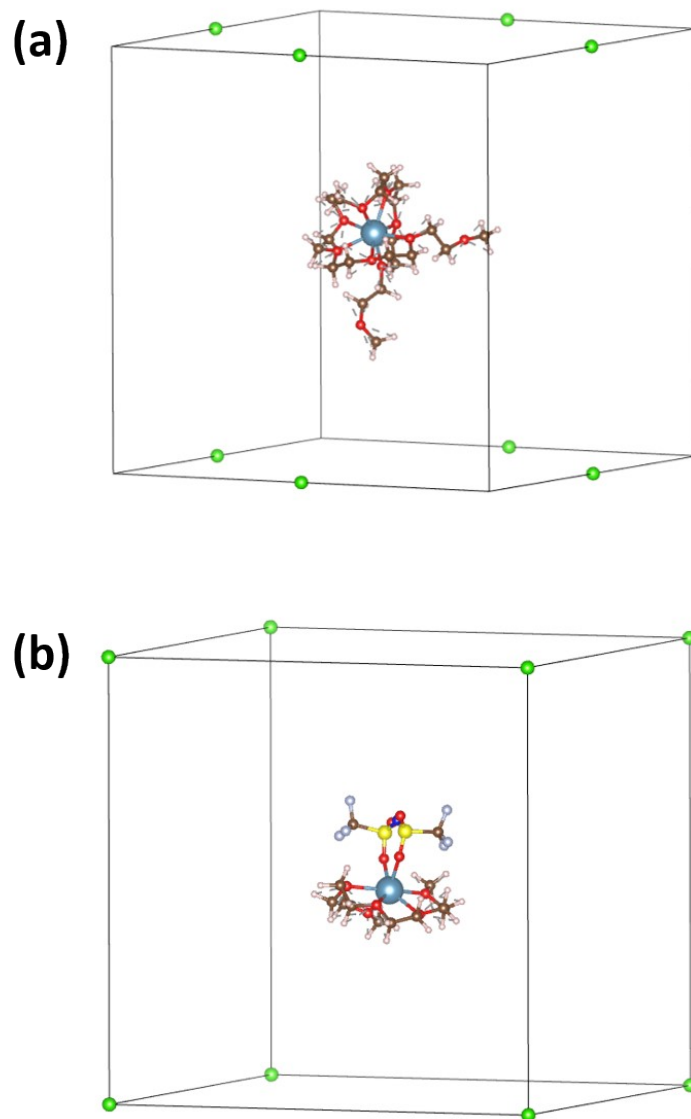
for the data treatment. In order to compare band intensities between spectra, all spectra were adjusted so that the C−H vibration bands' amplitudes in the 2700−3000 cm^{-1} range remained constant. The peak shapes were fit using Gaussian functions. The band's position was locked while the full width at half maximum and the peak height were refined. Temperature-controlled *in situ* experiments have been carried out in micro-Raman configuration (×50 objective lens) using a lab-made stainless-steel cell allowing heat treatment under Ar atmosphere. The samples were placed in a platinum crucible.

Theoretical details. One important requirement of our theoretical model is to capture the effect of solvent/salt concentration in solution, especially to account for the long-range electrostatic interactions between solvated species in such low-dielectric solvents. To this aim, periodic rather than molecular calculations were implemented, following the general framework described in our recent work.[1,2] The periodic boundary conditions indeed enabled simulating various salt concentrations to capture the composition-dependent electrostatic interactions between charged species at a moderate computational cost. The first coordination spheres of Ca^{2+} and the initial structure of $[Ca(TFSI)]^+$ ion-pair in tetraglyme solvent were constructed and pre-optimised in Avogadro[3], which were then used as inputs for DFT calculations performed using the Vienna *Ab Initio* Simulation Package (VASP)[4,5] within the framework of the Strongly Constrained and Appropriately Normed (SCAN) semi-local density functional[6]. The long-range van der Waals interactions were corrected using the revised Vydrov-van Voorhis nonlocal correction functional (rVV10).[7–9] The influence of outer solvent molecules on the first solvation sphere was taken into account using the Polarisable Continuum Model (PCM) provided in VASPSOL.[10,11] The PCM was parameterised with the solvent dielectric constant, which is ε_r = 7.50 for G4. The structural relaxations were performed in a (20 Å × 20 Å × 20 Å) unit cell and the energy at infinite dilution was extrapolated by varying the size of the simulation box up to 50 Å × 50 Å × 50 Å. The energy cut-off was set to 550 eV and the residual forces after structural relaxation were lower than 5·10^{-3} eV·Å^{-1}. The charged ions/molecules were generated by removing a corresponding number of electrons from the molecules. In order to mimic the ion−ion interaction and to better approach the enthalpy of reactions that occur in real solutions, energetic calculations were performed on the relaxed structures at different unit cell sizes, defined by $a \times a \times a$ Å^3, to establish the 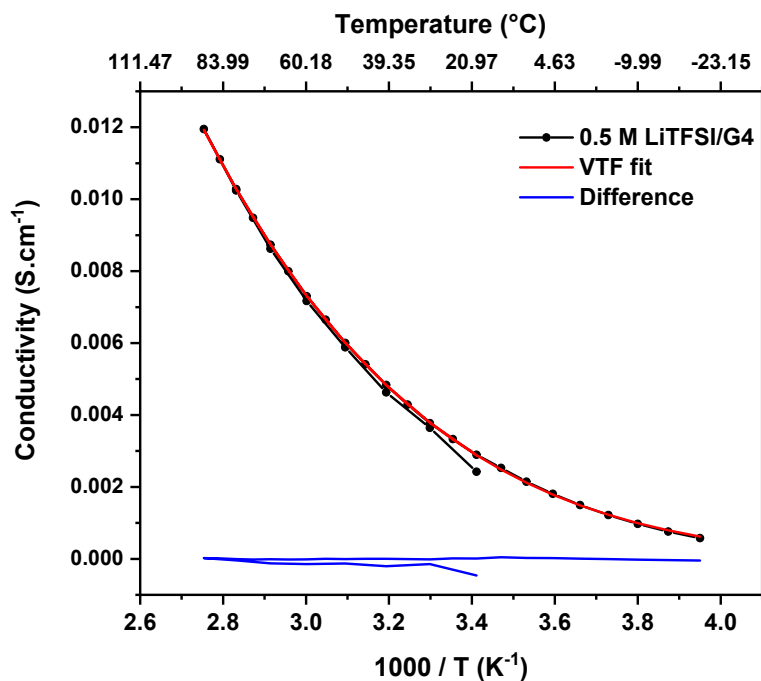relation between the energy of the charge-bearing ions and the size of the simulation box, $E = f(\frac{1}{a})$.[2,12] The molar concentration of the solution is related to the cell parameter of the simulation box by the equation $C_M = \frac{1661}{a^3}$ (with a in Å and C_M in
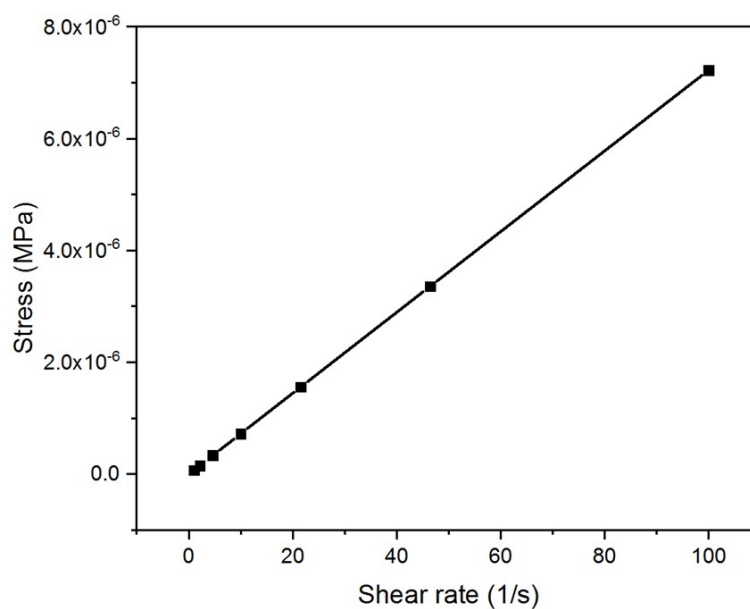
mol·L^{-1}). The simulation models of *mer*-[Ca(G4)$_2$]$^{2+}$ and [Ca(μ_2-TFSI)(G4)]$^+$ in the presence of Cl$^-$ anion, using as a punctual ion to localise the negative charge in the cell, are given in **Figure S1**. The energy of Cl$^-$ was subtracted from the system's total energy once the calculation converged. Molecular geometries and vibrational modes were visualised by VESTA and PyVibMS, respectively.[13,14]
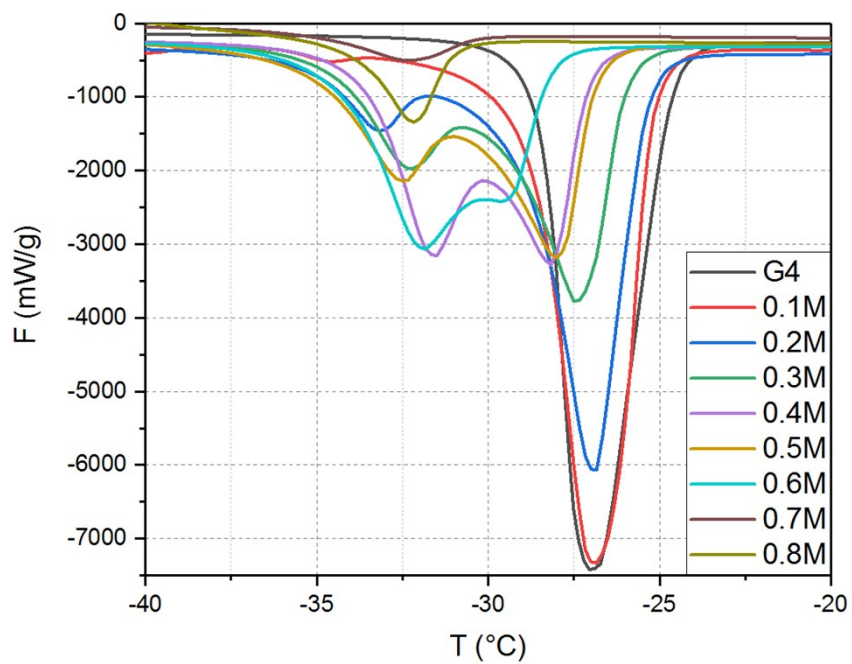

Figure S1. Simulation models of (a) *mer*-[Ca(G4)$_2$]$^{2+}$ and (b) [Ca(μ_2-TFSI)(G4)]$^+$ in the presence of Cl$^-$ counter-ions (Green spheres).

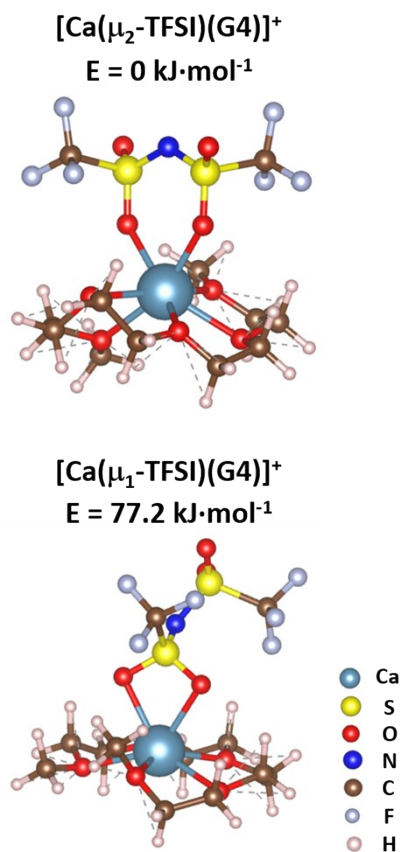**Figure S2.** VTF fit of the conductivity recorded on a 0.5 M LiTFSI/G4 solution.

Figure S3. Evolution in stress *vs* shear rate, recorded on a 0.7 M Ca(TFSI)$_2$/G4 solution. No threshold was detected, evidencing that Ca(TFSI)$_2$/G4 solutions behave as Newtonian liquid.

Figure S4. Differential scanning calorimetry results of $0 – 0.8$ M $Ca(TFSI)_2$/G4 solutions. The exothermic peaks indicate the crystallization process.
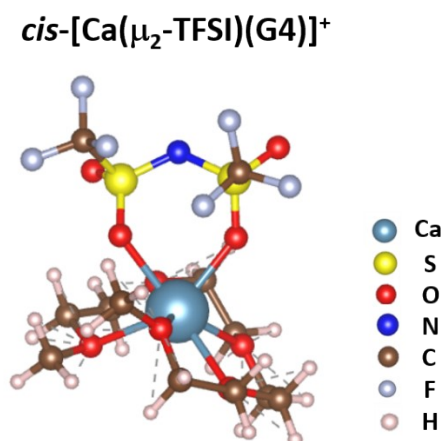
TFSI⁻ can exist in two different conformations *cis* and *trans*, which are defined by the relative position of two −CF$_3$ groups with respect to the O=S−N−S=O plane. In the solid-state, Ca(TFSI)$_2$·4H$_2$O contained exclusively TFSI⁻ ions in the *cis*-conformation coordinating to Ca^{2+} through their oxygen atoms.[15] Despite the presence of exclusive *cis*-TFSI⁻ in the solid-state, *cis* and *trans*-TFSI⁻ were detected when Ca(TFSI)$_2$ or Ca(TFSI)$_2$·4H$_2$O was dissolved in G4 solution, indicating a partial conversion of *cis* to *trans*-TFSI⁻ in the liquid phase.[1] In terms of thermodynamics, *trans*-TFSI⁻ is more stable than the *cis*-conformation by 1.6 kJ·mol^{-1} or 17 meV (calculated with the SCAN-rVV10 functional), and at ambient temperature, the thermal energy (25 meV) is sufficient to promote the inter-conversion of the two conformations. Furthermore, the expected population ratio between them is ~ 1/1, and thus both *cis*- and *trans*-TFSI⁻ can form contact ion-pairs with Ca^{2+}.

Figure S5. The optimised structures of *trans*-[Ca(μ_2-TFSI)(G4)]$^+$ and [Ca(μ_1-TFSI)(G4)]$^+$ ion-pairs calculated with the SCAN-rVV10 functional in the VASP code. [Ca(μ_1-TFSI)(G4)]$^+$ is less stable than *trans*-[Ca(μ_2-TFSI)(G4)]$^+$ by 77.2 kJ·mol^{-1}. The index following the μ character indicates the number of sulfur atoms involved in the coordination ring.
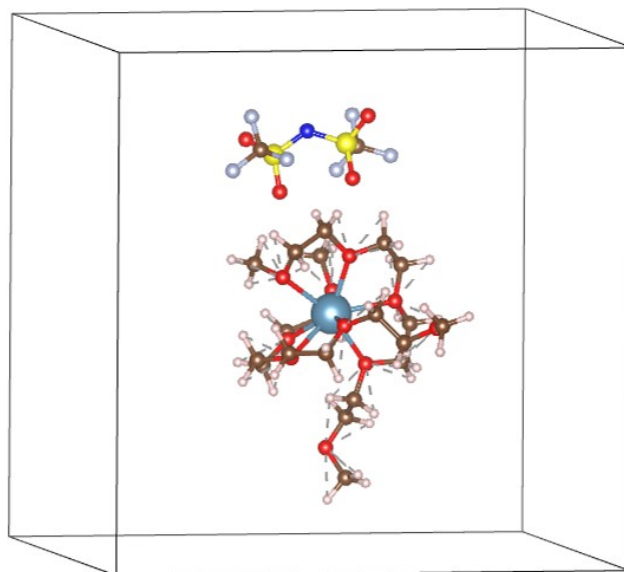
Due to the proximity of the oxygens in the structure, TFSI⁻ can act as a bidentate ligand. During the ion-pair formation process, the concomitant departure of one G4 molecule, the structural reorganization, and the arrival of TFSI⁻ are required. A combination of these three factors leads to a transformation of *mer*-[Ca(G4)$_2$]$^{2+}$ to [Ca(TFSI)(G4)]$^+$ and a coordination environment changing from [4+4] to [5+2] (**Figure 2**). When coordinating to a Ca^{2+} centre, the two oxygens that participated in the complexation can come from the same or two different sulfurs, and the resulting structures are denoted as [Ca(μ$_1$-TFSI)(G4)]$^+$ and *trans*-[Ca(μ$_2$-TFSI)(G4)]$^+$, respectively (**Figure S5**). The index following the μ character indicates the number of sulfur atoms involved in the coordination ring. The structural optimization performed with the SCAN-rVV10 functional in the VASP code reveals that [Ca(μ$_1$-TFSI)(G4)]$^+$ is less stable than *trans*-[Ca(μ$_2$-TFSI)(G4)]$^+$ by 77.2 kJ·mol^{-1}, due to the electrostatic repulsion originating from a short O···O distance (2.38 Å) and a great deformation in the $O\hat{S}O$ angle compared to a free TFSI⁻ ion (110.0° vs. 119.1°) (**Figure S5**).

Cis-[Ca(μ$_2$-TFSI)(G4)]$^+$ could also be found in solution, but it is less stable than the *trans*-isomer by 7 kJ·mol^{-1} (**Figure S6**). The Boltzmann population between *trans*-/*cis*-[Ca(μ$_2$-TFSI)(G4)]$^+$ is 13 at ambient temperature, and thus all the vibrational and thermodynamic properties would be dominated by those of *trans*-[Ca(μ$_2$-TFSI)(G4)]$^+$, which will be focused in the study.
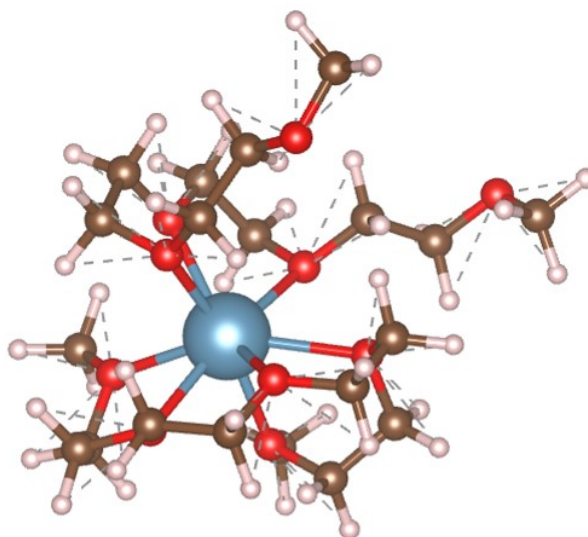
cis-[Ca(μ₂-TFSI)(G4)]⁺

Figure S6. Optimised structure of *cis*-[Ca(μ$_2$-TFSI)(G4)]$^+$ isomer. It is less stable than the *trans*-isomer by 70 meV (7.0 kJ·mol^{-1}). The molar ratio between the *trans*- and *cis*-isomer is 93/7 at ambient temperature.
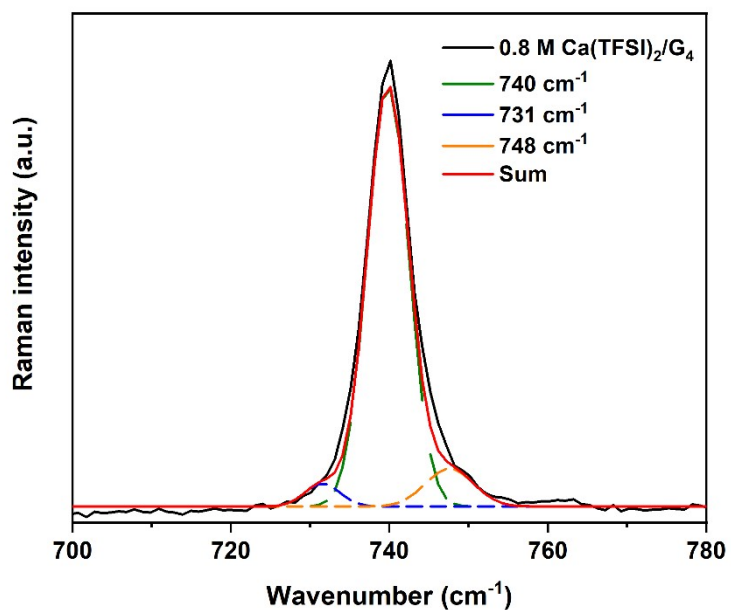
Figure S7. Optimised structure of solvent-separated ion-pair [*mer*-[Ca(G4)$_2$]//TFSI]$^+$. The structure was confined in a simulation box of 20 × 20 × 20 Å. The PCM was included to take into account the solvent effects.
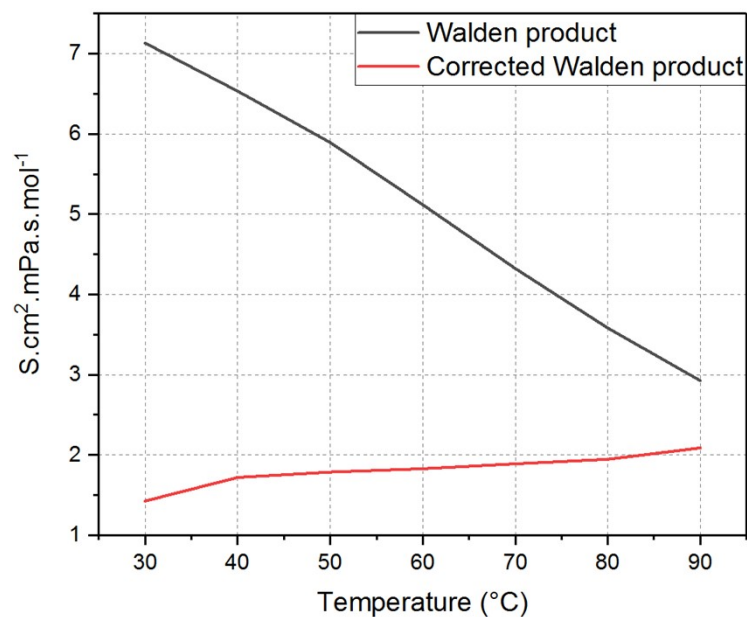

Figure S8. Solvation structure of [Ca(G4)$_2$]$^{2+}$ in the [5+3] coordination. At 0 K, this structure is less stable than *mer*-[Ca(G4)$_2$]$^{2+}$ by 37.7 kJ·mol^{-1}.
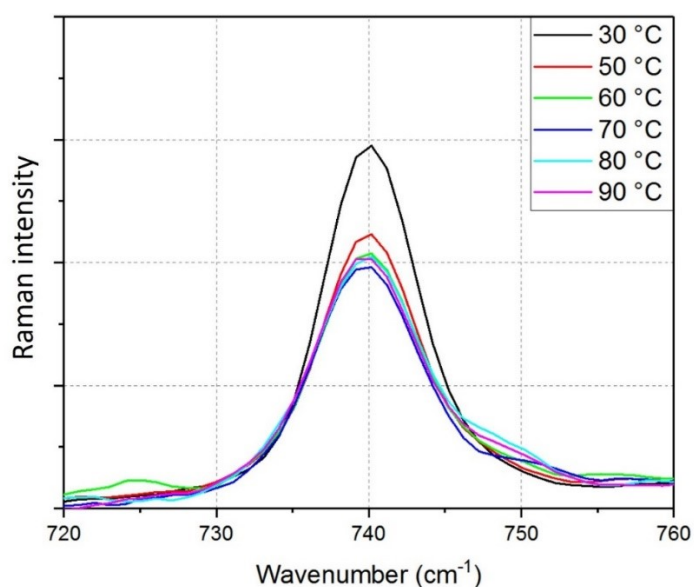
Figure S9. Deconvolution of TFSI$^-$ contraction-expansion mode at 740 cm^{-1} recorded on a 0.8 M Ca(TFSI)$_2$/G4 solution at 30°C.

Table S1. Integrated intensity (a.u.) of TFSI$^-$ vibration modes observed in 0.1 M to 0.8 M Ca(TFSI)$_2$/G4 solutions. The intensity ratio between the mode corresponding to coordinated TFSI$^-$ in the ion-pair and the one of free TFSI$^-$ is also given.

	0.1 M	0.2 M	0.3 M	0.4 M	0.5 M	0.6 M	0.7 M	0.8 M
731 cm^{-1}	0.078	0.333	0.557	0.791	0.918	1.069	1.249	1.468
740 cm^{-1}	2.139	6.819	13.915	18.916	24.987	25.740	32.485	37.493
749 cm^{-1}	0.482	1.111	1.671	2.277	2.564	3.204	3.902	4.526
Ratio	18.4 %	14.0 %	10.7 %	10.7 %	9.31 %	11.1 %	10.7 %	10.8 %

Figure S10. Corrected Walden product calculated for 0.1 M Ca(TFSI)$_2$/G4 solution. The uncorrected and corrected curves are represented as black and red lines, respectively. The corrected curve is calculated by $\frac{Peak\ area\ (Free\ TFSI)}{Peak\ area\ (Bound\ TFSI)} * \frac{\sigma\eta}{C}$. The amount of free and coordinated TFSI$^-$ is assumed to be proportional to the area of their characteristic peaks observed by Raman spectroscopy.

Figure S11. Evolution in the intensity of TFSI$^-$ contraction-expansion mode at 740 cm^{-1} recorded on a 0.2 M LiTFSI/G4 solution in the temperature-controlled Raman spectroscopy measurement.

Figure S12. Molecular representation of $[Mg(\mu_2\text{-TFSI})(G4)]^+$ ion-pair formation reaction.

Table S2. Energy of $Mg^{2+}-O$ interaction in different Mg^{2+} solvation structures with monoglyme, diglyme, triglyme, and tetraglyme. The structural relaxation was performed with the SCAN-rVV10 functional. The solvent effect was considered using the implicit solvent model included in the VASPsol code. All calculations were performed using the simulation box in the size of $20 \times 20 \times 20$ Å. The coordination number of each central ion is indicated in square brackets.

	Total M−O energy (kJ·mol⁻¹)	Energy per M−O bond (kJ·mol⁻¹)	Strain energy for Glyme (kJ·mol⁻¹)	Percentage of strain energy compared to M−O energy
$[Mg(G1)_3]^{2+}$ [2+2+2]	-1689.0	-281.5	101.8	6.0%
$[Mg(G2)_2]^{2+}$ [3+3]	-1674.0	-279.0	92.5	5.5%
$[Mg(G3)_2]^{2+}$ [3+3]	-1681.3	-280.2	110.2	6.6%
$[Mg(G4)]^{2+}$ [5]	-1529.1	-305.8	100.2	6.6%
$[Mg(G4)_2]^{2+}$ [3+3]	-1691.3	-281.9	130.1	7.7%

References:

1   L. H. B. Nguyen, T. Picard, N. Sergent, C. Raynaud, J.-S. Filhol and M.-L. Doublet, *Phys. Chem. Chem. Phys.*, 2021, **23**, 26120–26129.

2   A. K. Lautar, J. Bitenc, R. Dominko and J. S. Filhol, *ACS Appl. Mater. Interfaces*, 2021, **13**, 8263–8273.

3   M. D. Hanwell, D. E. Curtis, D. C. Lonie, T. Vandermeersch, E. Zurek and G. R. Hutchison, *J. Cheminform.*, 2012, **4**, 17.

4   G. Kresse and J. Furthmüller, *Phys. Rev. B - Condens. Matter Mater. Phys.*, 1996, **54**, 11169–11186.

5   G. Kresse and J. Furthmüller, *Comput. Mater. Sci.*, 1996, **6**, 15–50.

6   J. Sun, A. Ruzsinszky and J. Perdew, *Phys. Rev. Lett.*, 2015, **115**, 1–6.

7   H. Peng, Z. H. Yang, J. P. Perdew and J. Sun, *Phys. Rev. X*, 2016, **6**, 1–15.

8   J. Klimeš, D. R. Bowler and A. Michaelides, *J. Phys. Condens. Matter*, 2010, **22**, 022201.

9   J. Klimeš, D. R. Bowler and A. Michaelides, *Phys. Rev. B*, 2011, **83**, 195131.

10 M. Fishman, H. L. Zhuang, K. Mathew, W. Dirschka and R. G. Hennig, *Phys. Rev. B*, 2013, **87**, 245402.

11 K. Mathew, R. Sundararaman, K. Letchworth-Weaver, T. A. Arias and R. G. Hennig, *J. Chem. Phys.*, 2014, **140**, 0–8.

12 A. Kopač Lautar, A. Hagopian and J. S. Filhol, *Phys. Chem. Chem. Phys.*, 2020, **22**, 10569–10580.

13 K. Momma and F. Izumi, *J. Appl. Crystallogr.*, 2008, **41**, 653–658.

14 Y. Tao, W. Zou, S. Nanayakkara and E. Kraka, *J. Mol. Model.*, 2020, **26**, 290.

15 L. Xue, C. W. Padgett, D. D. DesMarteau and W. T. Pennington, *Solid State Sci.*, 2002, **4**, 1535–1545.